Astronomy & Astrophysics manuscript no. gordo_v1
May 2, 2019

Free-form lens model and mass estimation of the high redshift galaxy cluster ACT-CL J0102-4915, "El Gordo"

J.M. Diego[1,⋆], S.M. Molnar[2], C. Cerny[3], T. Broadhurst[4,5], R. Windhorst[6], A. Zitrin[7], R. Bouwens[8], D. Coe[9], C. Conselice[10], and K. Sharon[3]

[1] Instituto de Física de Cantabria (CSIC-UC). Avda. Los Castros s/n. 39005 Santander, Spain
[2] Institute of Astronomy and Astrophysics, Academia Sinica, P.O. Box 23-141, Taipei 10617, Taiwan
[3] Department of Astronomy, University of Michigan, 1085 South University Avenue, Ann Arbor, MI 48109
[4] Department of Theoretical Physics, University of the Basque Country, Bilbao E-48080, Spain
[5] Ikerbasque, Basque Foundation for Science, Alameda Urquijo, 36-5 Plaza Bizkaia E-48011, Bilbao, Spain
[6] School of Earth and Space Exploration, Arizona State University, Tempe, AZ 85287-1404, USA
[7] Department of Physics, Ben-Gurion University, Be'er-Sheva 84105, Israel
[8] Leiden Observatory, Leiden University, NL-2300 RA Leiden, The Netherlands
[9] Space Telescope Science Institute, Baltimore, MD, USA
[10] Centre for Astronomy and Particle Theory, School of Physics & Astronomy, University of Nottingham, Nottingham, NG7 2RD, UK

May 2, 2019

ABSTRACT

We examine the massive colliding cluster El Gordo, one of the most massive clusters at high redshift and with previous mass estimates close to (or even exceeding) the maximum mass allowed by standard cosmological models. We use a free-form lensing reconstruction method that avoids making assumptions about the mass distribution. We use data from the RELICS program and identify new multiply lensed system candidates. The new set of constraints provides a more precise mass estimate of this colliding cluster. By fitting a projected NFW mass distribution to the strong-lensing regime, we infer a total mass for the cluster of $M_{200c} = (1.35 \pm 0.15) \times 10^{15} M_{\odot}$, that is lower than earlier estimates and eases the claimed tension with LCDM models. We also find in our lens map a mass overdensity corresponding to the large cometary tail of hot gas, reinforcing its interpretation as a large tidal feature predicted by our hydrodynamical simulations. Finally, we discuss the observed relation between the plasma and the mass map, finding that the peak in the projected mass map may be associated with a large concentration of colder gas, exhibiting possible star formation. El Gordo is one of the first clusters that will be observed with JWST, which is expected to unveil new high redshift lensed galaxies around this interesting cluster, thus allowing us to improve on its mass estimation.

Key words. gravitational lensing – microlensing – dark matter – cosmology

1. Introduction

The galaxy cluster, ACT-CL J0102-4915, also known as *El Gordo* is a relatively high redshift z=0.870 with a rich, bimodal galaxy distribution (Williamson et al. 2011; Menanteau et al. 2012). Its mass has been estimated in earlier work using different techniques, including combined dynamical, X-ray and Sunyaev-Zeldovich (SZ) data (Menanteau et al. 2012), strong lensing data (Zitrin et al. 2013; Cerny et al. 2018), and weak lensing data (Jee et al. 2014). El Gordo has also been the subject of several dynamical studies, including numerical N-body simulations (Donnert 2014) and hydrodynamical simulations (Molnar & Broadhurst 2015; Zhang et al. 2015, 2018). These studies have highlighted the impressively large scale cometary structure visible clearly in X-ray images that appears to imply El Gordo is being observed right after a collision of two subgroups (Molnar & Broadhurst 2015; Zhang et al. 2015), similar to the iconic *Bullet* cluster. This interpretation is supported by the presence of two radio relics ahead and behind the X-ray cometary structure (Molnar & Broadhurst 2015; Lindner et al. 2014). Based on the X-ray and radio morphology, as well as on a preliminary lens model for the mass distribution, Ng et al. (2015) argue that El Gordo is in a return phase after first core passage. This means that the cluster is being observed after the phase of maximum apocenter, and that the two groups are moving against each other rather than away from each other. Part of this conclusion is based on a lens model that relies on weak lensing and that assigns more mass to the NW clump than to the SE clump. This interpretation is however challenged by lens models based on strong lensing data that place most of the mass in the SE group (Zitrin et al. 2013; Cerny et al. 2018).

The El Gordo cluster is an extreme cluster at several levels. It is the most massive cluster at $z \approx 0.9$ with an estimated mass ranging from $M_{200c} = 1.8{\times}10^{15} M_{\odot}$ to $M_{200c} = 2{\times}10^{15} M_{\odot}$. M_{200c} is the mass within the sphere of radius r_{200}. This radius is defined as the radius where the mass density enclosed in the sphere with the same radius and centered in the object is 200 times the critical density of the universe at the cluster redshift. Some authors estimate the overdensity in relation to the average density of the universe, $\rho_m = \rho_c \Omega_m$. In this case the mass is denoted as $M_{200\rho_m}$. Using SZ data, Williamson et al. (2011) estimates a mass of $M_{200\rho_m} = 1.89 \pm 0.45 \times 10^{15} M_{\odot}$. Menanteau et al. (2012) obtained a mass estimate of $M_{200\rho_m} = 2.16 \pm 0.32 \times 10^{15} M_{\odot}$ based on dif-

⋆ jdiego@ifca.unican.es

ferent scaling relations. Based on an extrapolation of the strong lensing mass model, Zitrin et al. (2013) estimate a total mass of $M_{200\rho_m} \sim 2.3 \times 10^{15} M_\odot$. Jee et al. (2014) uses weak lensing obtained with HST and estimates $M_{200c} = 3.13 \pm 0.56 \times 10^{15} M_\odot$.

At the high-end of the mass range for El Gordo, these masses are in tension with the standard LCDM model (see for instance Jee et al. 2014), that predicts the maximum mass at this redshift should be less than $M_{200\rho_m} \approx 1.7 \times 10^{15} M_\odot$ (Harrison & Coles 2012). A similar conclusion is reached when studying the results obtained by large N-body simulations. Using the very large 630 Gpc^3 N-body simulation Jubilee (based on a standard LCDM model), Watson et al. (2014) (in their Figure 5) find that the most massive cluster in the simulation and at $z = 0.9$ is $M_{200\rho_m} \approx 1.5 \times 10^{15} M_\odot$. Note that in Watson et al. (2014), the masses are defined as $M_{178\rho_m}$ rather than $M_{200\rho_m}$ or M_{200c}. For an NFW profile, $M_{178\rho_m} \approx 1.2 M_{200c}$ and $M_{178\rho_m} \approx 4\%$ times higher than $M_{200\rho_m}$ (Waizmann et al. 2012). Given the fact that El Gordo was found in a relatively small area of the sky, it raises the question about its significance as possible evidence for tension with the LCDM model. At the source of this apparent tension could be an overestimation of its mass. Hence, it is important to improve on its mass estimation using the latest lensing data.

As of 2014, El Gordo was also the highest-redshift cluster known to host radio relics (Lindner et al. 2014). The X-ray emission exhibits an interesting offset between the peak of the X-ray emission and the position of the BCG. Contrary to what happens in the Bullet cluster, the X-ray peak seems to be ahead of the BCG. However, in the interpretation of Ng et al. (2015), the BCG would be moving towards the second group, so the X-ray peak would be trailing the BCG. The returning phase interpretation of El Gordo is challenged based on results from dedicated N-body/hydrodynamical simulations reproducing most of the observations of El Gordo (Molnar & Broadhurst 2015; Zhang et al. 2015). Also Molnar & Broadhurst (2018) demonstrate that the speed of the outgoing shocks can be very large (4000–5000 km s^{-1}) in a massive merging cluster like El Gordo, therefore leaving the system before the first turnaround.

El Gordo is also unique in the sense that it is a powerful lens at relatively high redshift. One of the features that makes El Gordo an attractive target for lensing studies is the fact that for sources at high redshift, critical curves form at relatively large distances from the member galaxies. This is particularly true in the gap between the two clusters, where the critical curves are relatively undisturbed by nearby member galaxies. Having undisturbed critical curves is relevant to observe caustic crossing events of distant stars (Kelly et al. 2018; Diego et al. 2018), since in this case the maximum magnification can be larger than in situations where critical curves are affected by microlenses in member galaxies or from the intracluster medium. Caustic crossing events has been proposed as a technique useful to study Pop III stars and stellar-mass black hole accretion discs in Windhorst et al. (2018) with JWST. Because El Gordo is the highest redshift known cluster with potentially such significant transverse motion — based on the X-ray morphology and the two lensing mass centers discussed in this paper — it is an ideal target for JWST follow-up to search for caustic transits at z>>1, and possibly for First Light caustic transits at z>7. For this reason, El Gordo is a JWST GTO target that will be observed in Cycle 1 (JWST program # 1176; PI: Windhorst). It is our sincere hope that JWST Guest Observers will propose to observe El Gordo in many successive epochs, amongst others to find caustic transits at z>>1.

In this paper we derive the mass distribution and study this interesting cluster using the latest data from the RELICS program and newly identified strong lensing systems. We use our free-form lensing reconstruction code WSLAP+ (Diego et al. 2005a, 2007; Sendra et al. 2014; Diego et al. 2016), which does not rely on assumptions about the distribution of dark matter. We pay special attention to the integrated mass as a function of radius and the effect that extrapolations of the derived mass profile up to the virial radius has on the inferred total mass of the cluster.

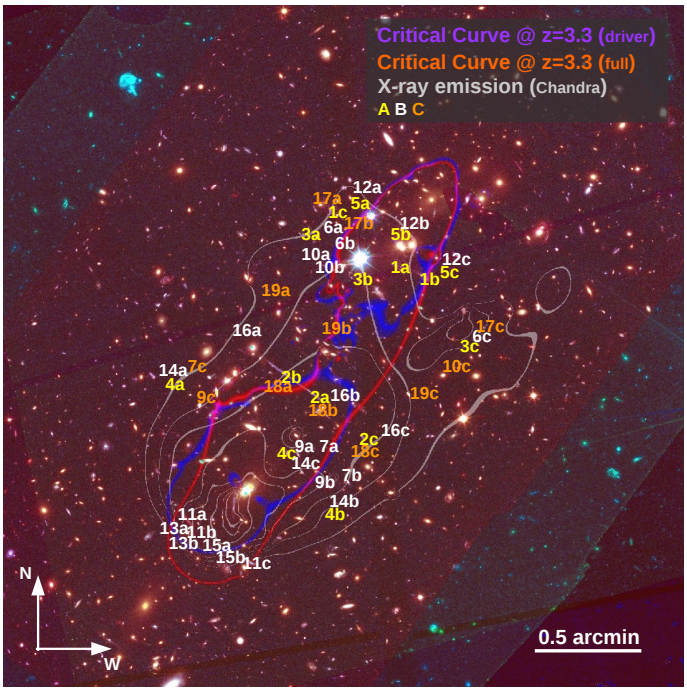

Fig. 1. HST Optical+IR composite image with overlaid contours from Chandra. Multiply lensed images are marked with their corresponding IDs. The color of the IDs indicate the quality of the family identification. Images with yellow IDs are category A (reliable), IDs in white are still reliable, but not as confident as A. Images with IDs in orange are less reliable although still valid candidates. The blue and red curves show the critical curve at $z = 3.3$ for the driver model (derived from images in category A) and full model (derived from images in categories A and B) respectively.

This paper is organized as follows. In section 2 we describe the data and simulations used in this work. In section 3 we describe briefly the algorithm used to perform the lensing reconstruction. Results are presented in section 4 and discussed in section 5. We summarize and conclude in section 6. We adopt a standard flat cosmological model with $\Omega_m = 0.3$ and $h = 0.7$. At the redshift of the lens, and for this cosmological model, one arcsecond corresponds to 7.8 kpc.

2. Observational and simulated data

In this section we describe briefly the data used in this work as well as previous N-body simulations of El Gordo cluster that will be used to compare with our results.

2.1. Optical data

We use public Hubble imaging data from programs GO 12755 (PI J. Hughes), GO 12477 (PI F. High), and GO 14096 (PI D. Coe). These ACS and WFC3/IR observations include data in 10 filters spanning wavelengths *sim*0.4–1.7 μm. The Reionization Lensing Cluster Survey (RELICS; Coe et al. 2019) delivered reduced images combining data from all of these HST pro-

grams, including their own (14096). RELICS also delivered photometric redshift catalogs of objects detected in these images. We retrieved these data products from the Mikulski Archive for Space Telescope (MAST). From the reduced images, we produce colour images by combining the optical and IR bands.

2.2. X-ray data

To explore the dynamical state of El Gordo, we also produce an X-ray image using public Chandra data. In particular, we used data from the ACIS instrument acquired in 2011–2012 and with the Obs ID 12258, Obs ID 14022 and Obs ID 14023 (PI. J. Hughes) totaling $\approx$ 350 ks. The X-ray data is smoothed using the code ASMOOTH (Ebeling et al. 2006). A false color image from the HFF imaging overlaid contours of the smoothed X-ray data is shown in figure 1. The distribution of X-rays shows a cometary structure similar to the Bullet cluster. The peak of the X-ray emission is offset with respect to the BCG by $\approx$ 70 kpc.

2.3. Simulated data

In order to study the impact of extrapolating a strong lensing derived profile (i.e, a profile that extends a limited range in radii) up to the virial radius, we use dedicated N-body/hydrodynamical simulations that mimic El Gordo (for details of the simulations see Molnar & Broadhurst 2015). Our simulations were constrained by multi-frequency data: X-ray, radio (Sunyaev–Zel'dovich observations), and optical (for gravitational lensing and dynamics). Our best model for El Gordo assumed initial total masses of $1.4{\times}10^{15}$ $M_\odot$ and $7.5{\times}10^{14}$ $M_\odot$ for the main and the infalling cluster respectively, an impact parameter of 300 kpc, and a relative initial infall velocity of 2250 km/sec when separated by the sum of the two virial radii. This model explains most of the observed features of El Gordo: the distinctive cometary feature with a *twin-tailed* wake observed in the X-ray morphology, the locations of the two peaks of the dark matter components, and the position of the SZ peak. In this paper we use the total mass distribution from our best model to derive the surface mass distribution, and compare that to the surface mass distribution we derived from gravitational lensing.

2.4. Multiply lensed galaxies

In this section we discuss the lensed systems used to constrain the mass model. The identification of multiply lensed galaxies systems in El Gordo is particularly challenging, particularly because no multiply lensed galaxies with spectroscopic redshifts have been confirmed so far. However, with the new RELICS data, we can improve upon previous identifications. As a default, we adopt the original naming scheme of Zitrin et al. (2013) for the lensed system candidates, who identified the first families of strongly lensed galaxies and performed the first strong lensing analysis of this cluster based on the three HST bands available at the time (the compilation of systems is detailed in the appendix). Notably, two systems (1 and 2 in Fig. 1) exhibit well resolved morphological features that, together with robust photometric redshifts, allow to unambiguously confirm these two families of images. Systems 3, 4 and 5 contain also morphological information and reliable photometric redshifts, which makes the identification of these systems equally robust. Systems 1 through 4 are similar to the systems defined in Zitrin et al. (2013), and Cerny et al. (2018). We note that systems 10 and 20 in Cerny et al. (2018) are part of our systems 1 and 2, where we identify different knots in the systems that are used as additional constraints. Our new system 5 was also independently identified by Cerny et al. (2018) as system 13 in their work. In the original scheme of Zitrin et al. (2013), system 4 was composed of 3 counterimages, and two possible radial images. A preliminary model clearly disfavors the radial image 4.2 and candidate image 4.3 (in Zitrin et al. 2013) as part of system 4. We note that Cerny et al. (2018) also rejected these two counterimages as part of system 4 (as do some updated models by Zitrin et al.; *private communication*). Instead, we suggest that the two alleged arclets 4.2 and 4.3 in Zitrin et al. (2013) are likely features in the galaxy cluster associated with the cooling of the plasma (see Section5.2). Using the robust systems 1 through 5 we derive a first model based on these reliable systems. This model is later used to unveil new system families (listed in Table A.1). We refer to this first model for the mass distribution as the *driver model*.

Table A.1 lists all the arclets, including also some candidates listed here for completeness, but not used in the lens reconstruction. Also for completeness, we include system 8 as originally defined in Zitrin et al. (2013). The driver model disfavors this system, so we do not include in our lens reconstruction. Also Cerny et al. (2018) discarded this system. The systems in table A.1 are divided in 3 categories, A, B and C. Arclets in category A are robustly confirmed based on their color, morphology and photometric redshift. As mentioned above, we use these arclets to derive the driver model. Systems in category B are highly compatible with the driver model. In addition, color, morphology and when available the photometric redshift is also consistent among the different members of the same family of images. Systems labeled A and B are used to derive an alternative model that we name the *full model*. Arclets in the category C are still consistent with the driver model, but lack of morphological information, a mismatch in the alignment of the predicted image (compared with the observed one), or tension between the predicted and observed magnification ratios reduces the reliability of the identification. Arclets marked with label C are not used in the mass reconstruction, but are still included in table A.1. Future data will confirm or reject these system candidates.

The systems in table A.1 that are new identifications are marked with bold face. Systems that were fully included in previous work are indicated in the *Comments* column. Our new system 6 has an estimated redshift (from the lens model) of $z \approx 4.3$, which is consistent with the photometric redshift. For system 7, we identify a new candidate for 7c that differs from the candidate in Zitrin et al. (2013). System 10 is a new system with a photometric redshift of 5.1 (for 10a). The driver model is fully consistent with this system and redshift. System 11 is a new redefinition of system 5 in Zitrin et al. (2013). The driver model suggests that the big arclet forming part of system 5 in Zitrin et al. (2013) consists of two images merging at the critical curve. The corresponding third image is identified with the tail of a bright galaxy (see Figure 5). Based on the driver model, the redshift of this galaxy should be $z \approx 3.1$ while the photometric redshift for the arc is $z \approx 2.2$. When this system is included in the lens reconstruction (i.e in the full model), we adopt the photometric redshift for this system. System 12 is a redefinition of system 14 in Cerny et al. (2018), based on the driver model and color+morphological information. Our 12a matches 14a in Cerny et al. (2018), but we identify two different counterimages. The driver model predicts a redshift of $z \approx 3$, consistent with the photometric redshift of $z = 3.4$ of 12a. System 13 has no photometric redshift. The driver model predicts a redshift $z = 3$

for this system. System 14 has a photometric redshift $z = 2.7$ (14a), but we adopt the redshift predicted by the driver model, i.e $z = 4$, for this system. System 15 corresponds to system 8 in Cerny et al. (2018), which was also independently identified. Both the photometric redshift ($z = 2.7$) and the redshift predicted by the driver model ($z = 2.65$) agree reasonably well. Systems 17, 18 and 19 are all new candidates, but lack of morphological features do not allow us to confirm their association based on the morphology of the predicted images.

Finally, we do not consider system 5 in Cerny et al. (2018). Although the driver model is consistent with the positions of system 5 in Cerny et al. (2018), a third image is clearly predicted, but not observed, casting doubt on the feasibility of this system. However, we should note that it is also possible that the driver model fails at correctly predicting the position of the third counterimage, and that this image could be hidden underneath one of the bright member galaxies.

3. Formalism

The mass reconstruction is based on our method WSLAP+. The reader can find the details of the method in our previous papers (Diego et al. 2005a, 2007; Sendra et al. 2014; Diego et al. 2016). Here we give a brief summary of the most essential elements. The lens equation is defined as follows,

$$\beta = \theta - \alpha(\theta, \Sigma), \tag{1}$$

where θ is the observed position of the source, α is the deflection angle, $\Sigma(\theta)$ is the surface mass-density of the cluster at the position θ, and β is the position of the background source. Both the strong lensing and weak lensing observables can be expressed in terms of derivatives of the lensing potential:[1]

$$\psi(\theta) = \frac{4GD_l D_{ls}}{c^2 D_s} \int d^2\theta' \Sigma(\theta') ln(|\theta - \theta'|), \tag{2}$$

where D_l, D_s, and D_{ls} are the angular diameter distances to the lens, to the source and from the lens to the source, respectively. The unknowns of the lensing problem are in general the surface mass density and the positions of the background sources in the source plane. The surface mass density is described by the combination of two components; i) a soft (or diffuse) component (usually parameterized as superposition of Gaussians); and ii) a compact component that accounts for the mass associated with the individual halos (galaxies) in the cluster.
For the diffuse component, different bases can be used but we find that Gaussian functions provide a good compromise between the desired compactness and smoothness of the basis function. A Gaussian basis offers several advantages, including a fast analytical computation of the integrated mass for a given radius, a smooth nearly constant amplitude between overlapping Gaussians (with equal amplitudes) located at the right distances, and a orthogonality between relatively distant Gaussians that help reduce unwanted correlations. For the compact component, we adopt directly the light distribution in the IR band (F160W). For each galaxy, we assign a mass proportional to its surface brightness. This mass is later re-adjusted as part of the optimization process.

As shown by Diego et al. (2005a, 2007), the strong and weak lensing problem can be expressed as a system of linear equations that can be represented in a compact form,

$$\Theta = \mathbf{\Gamma} X, \tag{3}$$

[1] Note however, that through observations one measures the reduced shear, $\gamma_r = \gamma/(1-\kappa)$ where κ is the convergence.

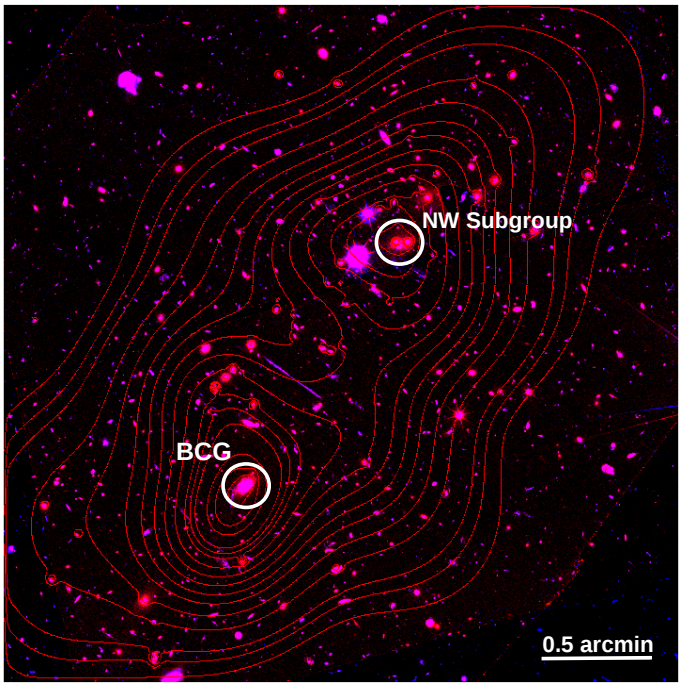

Fig. 2. Contours of the mass distribution for the full model compared with the optical image. The circles mark the position of the BCG in the SE and the center of the NW group.

where the measured strong lensing observables (and weak lensing if available) are contained in the array Θ of dimension $N_\Theta = 2N_{\rm sl}$, the unknown surface mass density and source positions are in the array X of dimension

$$N_{\rm X} = N_{\rm c} + N_{\rm g} + 2N_{\rm sl} \tag{4}$$

and the matrix $\mathbf{\Gamma}$ is known (for a given grid configuration and fiducial galaxy deflection field) and has dimension $N_\Theta \times N_{\rm X}$. $N_{\rm sl}$ is the number of strong lensing observables (each one contributing with two constraints, x, and y), and $N_{\rm c}$ is the number of grid points (or cells) that we use to divide the field of view. Each grid point contains a Gaussian function. The width of the Gaussians are chosen in such a way that two neighbouring grid points with the same amplitude produce a horizontal plateau in between the two overlapping Gaussians. In this work, we consider only regular grid configurations. Irregular grids are useful when there is a clear peak in the mass distribution, for instance when the cluster has a well defined centre or a single BCG. $N_{\rm g}$ (in Eq. 4) is the number of deflection fields (from cluster members) that we consider. $N_{\rm g}$ can be seen as a number of mass layers, each one containing one or several galaxies at the distance of the cluster. In this work we set $N_{\rm g}$ equal to 1, i.e, all galaxies are forced to have the same mass-to-light ratio.

Finally, $N_{\rm s}$ in Eq. 4 is the number of background sources (each contributes with two unknowns, β_x, and β_y), which in our particular case ranges from $N_{\rm s} = 5$ when only the subset of reliable systems are used (driver model in section 2) to $N_{\rm s} = 16$, when all systems labeled A or B in Table A.1 are used in the reconstruction (full model). The solution, X, of the system of equations 3 is found after minimising a quadratic function of X (derived from the system of equations 3 as described in Diego et al. 2005a). The minimisation of the quadratic function is done with the constraint that the solution, X, must be positive. Since the vector X contains the grid masses, the re-normalisation factors for the galaxy deflection field and the background source positions, and all these quantities are always positive (the zero of the

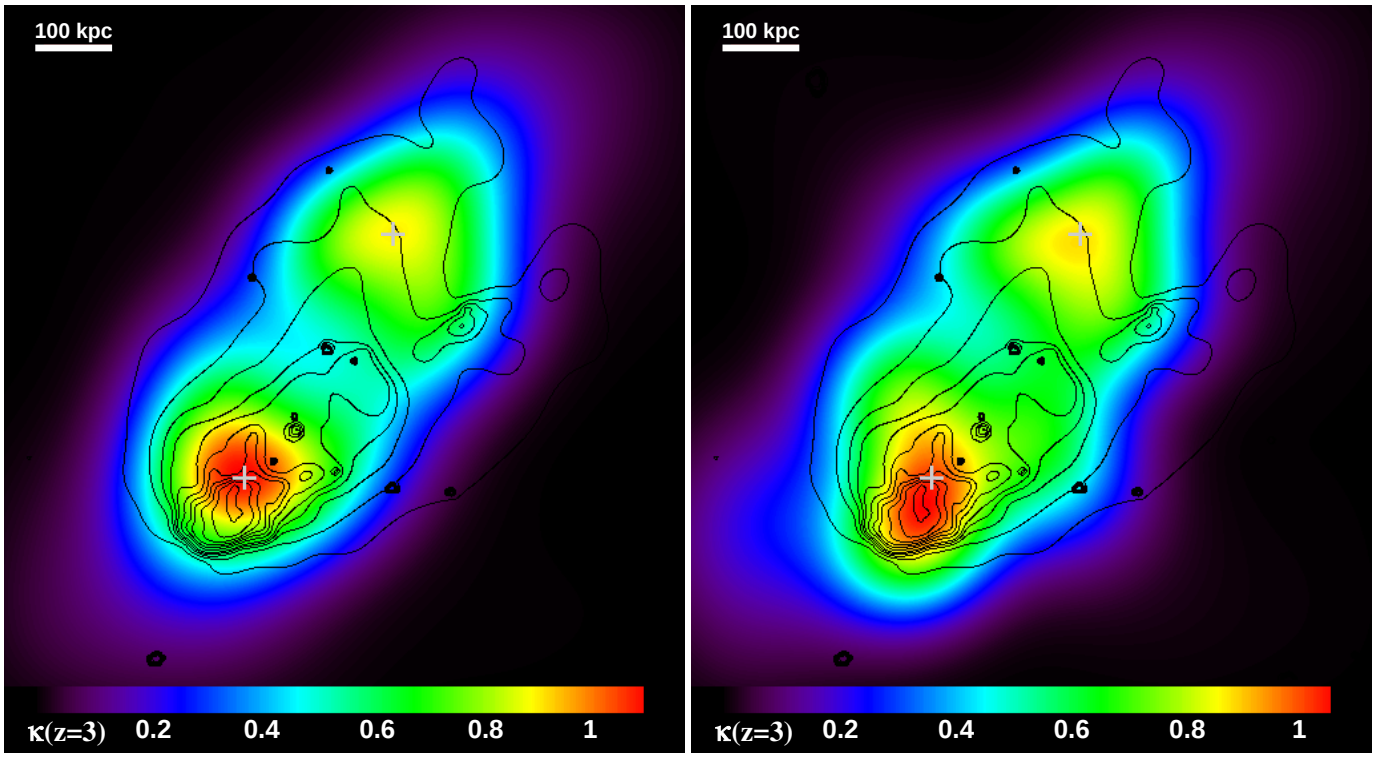

Fig. 3. Left panel. Convergence (color scale at z=3) vs X-ray contours (contours) for the driver model. The converge has the contribution from the member galaxies removed. The crosses mark the position of the BCG and NW group. Right panel. Similar as the left panel, but for the full model. Note the good correlation between the X-ray and SE mass peak.

source positions is defined in the bottom left corner of the field of view). Imposing $X > \mathbf{0}$ helps constrain the space of meaningful solutions, and to regularise the solution, as it avoids large negative and positive contiguous fluctuations. The quadratic algorithm convergence is fast (a few minutes), allowing for multiple solutions to be explored in a relatively short time. Different solutions can be obtained after modifying the starting point in the optimization and/or the redshifts of the systems without spectroscopic redshift. A detailed discussion of the quadratic algorithm can be found in Diego et al. (2005a). For a discussion of its convergence and performance (based on simulated data), see Sendra et al. (2014).

4. Results

Thanks to the new RELICS data we can revise the multiple images identification in this cluster and assign them a rank ranging from A (most reliable) to C (least reliable). Based on the set of images ranked A (see Table A.1) we derive the driver model, which is later used to uncover new multiply images, or to reveal issues with previous identifications. Even though the driver model is based on a relatively small subset of only 5 families of images, the spatial distribution of these 5 families allows us to derive a reliable lens model. The driver model disfavors the radial counterimages candidates 4.2 and 4.3 in Zitrin et al. (2013) (these images were discarded also by Cerny et al. 2018), and instead we suggest these may be signatures of cooling flows or jets near the BCG (see Section 5.2 for discussion). System 8 in Zitrin et al. (2013) shows a relative good consistency with the driver model in terms of predicted vs observed positions, but the morphology of the observed images does not match well with the predicted morphology, so we do not use this system in any of our lensing reconstructions as well (this systems is still included in Table A.1 for completeness). Some of the counterimages postulated in earlier work as candidates (for instance 7c and 9c) are in general consistent in terms of position, but their morphology is not well reproduced by the lens model. We also unveil new image candidates, some of them independently identified in Cerny et al. (2018).

In addition to these, we identify additional new families as described in the appendix. System 15 in Cerny et al. (2018) is consistent with the driver model, but a third image is clearly predicted by the driver model and not observed. Consequently, we do not use this system in our reconstruction, although we should note that the predicted position for the third image is only a few arcseconds from the BCG. Hence, it is possible that the driver model is not accurate enough around the BCG, and that the third image lies buried behind the bright BCG, and with a smaller magnification than the one predicted by the driver model. A smaller magnification is possible if the BCG has a larger mass-to-light ratio in the central region, for instance through a central spike in the mass distribution or a supermassive black hole at the centre.

Based on the driver model, we expand the number of reliable systems and estimate their redshifts based on the available photometric redshift information and/or the redshift predicted by the driver model. Using the expanded set of systems (ranked A and B in Table A.1), we derive a new model, the *full* model. The mass distributions of the two models are compared in Figure 3. For these plots, we have subtracted the contribution from the member galaxies to better show the diffuse component. The two models look similar to first order, but some differences can be appreciated specially around the BCG, where the full model places the peak of the diffuse component at several arcseconds from the BCG. In particular, the peak of the soft component correlates very well with the peak in the X-ray emission. Similar correla-

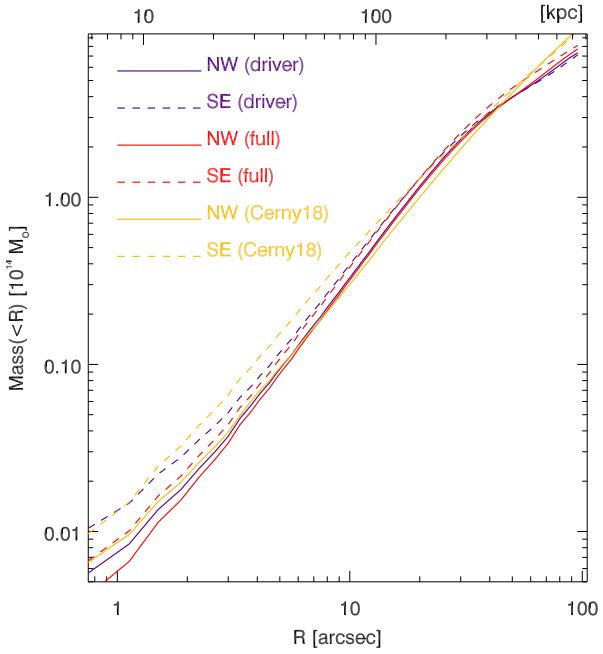

Fig. 4. Integrated mass as a function of aperture radius. The purple lines correspond to the driver model, the red lines correspond to the model derived with all arcs. For comparison we show also the corresponding integrated mass for the mass model from Cerny et al. (2018) as orange lines. In all cases, the solid lines are for profiles centered in the NW group while the dashed lines are for profiles centered in the SE BCG.

tions between the diffuse component obtained by our method and the observed X-ray emission were found in earlier work, where we discussed the possibility that the lensing data is sensitive also to the plasma mass. This possibility is discussed in more detail in section 5.2.

In terms of integrated mass, both models look also similar, but with the full model having slightly more mass, specially on the SE group. A quantitative comparison of the integrated mass as a function of radius for each subgroup and the two models is presented in Figure 4. The mass increase in the SE group is due mostly to the smaller photometric redshift of system 11 used to derive the full model compared with the larger redshift predicted by the driver model. Figure 5 shows the predicted images for 11a and 11b based on 11c for the driver model and the full model. The driver model does a good job at predicting the arc position and morphology for a source redshift of ≈ 3. In the full model, the system is assumed to be at the photometric redshift of $z = 2.2$ instead, which results in a mass increase in the SE group needed to compensate for the smaller redshift of the background source.

4.1. Comparison with earlier results

In this section we compare our models with previous results derived from the same RELICS data and presented in Cerny et al. (2018). We should note that the constraints used on this work and in Cerny et al. (2018) are not exactly the same, so some of the differences can be attributed to this fact. Our lensed candidates were derived independently from Cerny et al. (2018), although in some cases, our system candidates coincide, but not in all cases. System 3, with photometric redshift $z = 7.42$ in Cerny et al. (2018), is claimed to be a newly identified system. However, the positions of 3.1, 3.2 and 3.3 are very similar (within a fraction of an arcsec) with the positions of system 3 in Zitrin et al. (2013), but in this case, with a different photometric redshift of 4.16. For the position and redshift of system 3, we adopt the values of Zitrin et al. (2013) based on the color of the images and positions relative to the critical curve of preliminary models. We have not used system 8 from Cerny et al. (2018). System 8 appears as a likely multiple lensed arc with two pairs of images very close to each other and possibly merging around a critical curve. System 10 in Cerny et al. (2018) is included as an extra knot in our system 1. Similarly, we have included the positions of system 20 of Cerny et al. (2018) as additional knots of system 2. For the driver model, all systems are included also in Cerny et al. (2018) (although, see the difference in redshift for system 3). For the alternative full model, we include all systems used in Cerny et al. (2018), except system 8 as mentioned above. In the full model, we also include systems not included in Cerny et al. (2018). These are the new system candidates 6, 10, 13, 14 and 16 and the redefined system candidates 11, 12 and 14 listed in the table in appendix. The system 14 in Cerny et al. (2018) was not included in their model. Here we use a redefined version of this system as our new system 12.

The critical curves of our two models and the model in Cerny et al. (2018) are compared in Figure 6. The position of the critical curves is consistent between both models, although our model predicts slightly wider critical curves, suggesting a rounder distribution for the projected surface mass density in our model. In contrast, Cerny et al. (2018) predicts a narrower distribution of matter, with the mass being more concentrated around the line intersecting the two clumps. The models show a better agreement (in terms of positions of the critical curve) around the position of the constraints. The figure shows the estimated observed position of the critical curve based on symmetry arguments for the giant arc of system 2 (at $z \approx 3.3$). All models agree relatively well with this position by placing the critical curve (at the redshift of system 2) very close, or intersecting, the estimated position of the critical curve. In the South-East part of the lens, differences between models are larger, reflecting the relative smaller density of constraints in this part of the lens (see Figure 1), but possibly also the fact that parametric methods assume explicit mass profiles that can extend the mass distribution beyond the range of distances covered by the lensing constraints. A more quantitative comparison of the magnification between the different models can be made by comparing the curves, $A(>\mu)$, of the area above a given magnification. These curves are computed by integrating the differential area curves, i.e $A(>\mu) = \int_{mu}^{\mu_{max}} d\mu dA/d\mu$ where μ_{max} is the maximum magnification considered (220 in this case) and $dA/d\mu$ is the area in the lens plane with magnification μ and in the interval $d\mu$, divided by the magnification μ (i.e, the corresponding area in the source plane). The curves $A(>\mu)$ follow the usual $A_o\mu^{-2}$ above magnification $\mu \approx 10$. The values of the normalization for the different models and at $z_s = 3.3$ are (in arcmin^2): $A_o = 4.5$ (Cerny18 model), $A_o = 10$ (driver model) and $A_o = 8.5$ (full model). $A(>\mu)$ can be interpreted as the probability of a galaxy being lensed by a factor larger than μ. At high magnifications, the driver and full models predict about twice the probability compared with the model in Cerny et al. (2018). This difference is mostly due to the shallower profiles in the driver and full models around the position of the critical curves. The values of A_o put El Gordo at a level comparable to other powerful lenses, like the Hubble Frontier Fields clusters, in terms of lensing efficiency (see Vega-Ferrero et al. 2019 (accepted)). This means that future observations, like the planned ones with JWST, promise to reveal many additional high-redshift lensed galaxies.

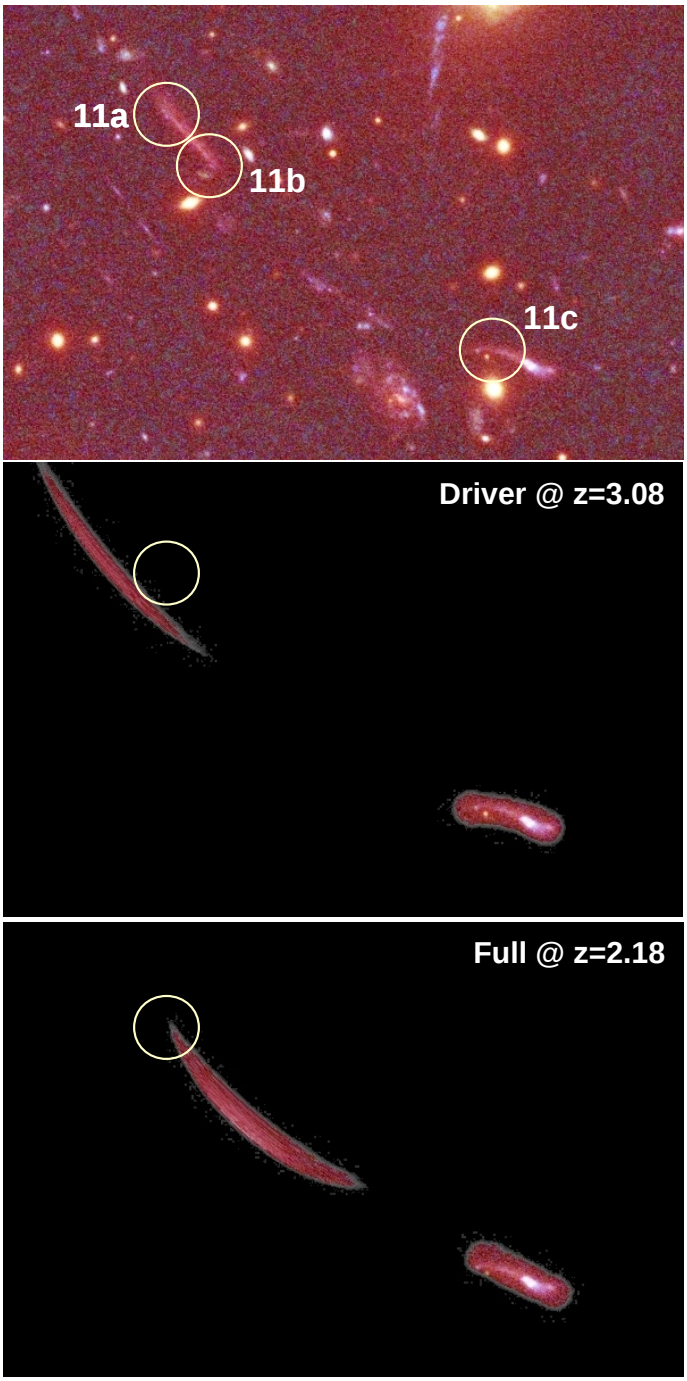

Fig. 5. The top panel shows the proposed redefinition of the original system 5 in Zitrin et al. (2013) as the new system 11. The middle panel shows the predicted merging arc by the driver model assuming the background galaxy is at z=3.08. The bottom panel shows the corresponding prediction made by the full model when the source is forced to be at the photometric redshift. The white circle in the middle and bottom panel marks the position of 11a.

Due to the relatively large separation between the two groups, the critical curve on the Central-East side of the cluster is relatively unperturbed by cluster members (this can be appreciated in Figure 1 where the critical curves are very smooth in this part of the cluster). At even higher redshift, the critical curves move outwards where the distortion by cluster members is expected to be even smaller. This has important implications for the probability of observing caustic crossing events of distant stars, for instance Pop III stars at $z > 7$ as suggested by Windhorst et al. (2018). Pristine critical curves (that is, critical curves which are not perturbed by microlensing from stars or remnants in the cluster members or in the intracluster medium) can host lensed images in their vicinity with magnifications factors of order 10^6 when the background source has the size of a Pop III star. In contrast, critical curves that are close to the cluster centre (for instance, for background objects at relatively low redshifts of $z \approx 2$ or less) are normally perturbed by such microlenses resulting in maximum magnification factors of order 10^4 for background sources with sizes comparable to giant stars (see for instance Diego 2018, for details).

In terms of total mass, the agreement between the models is made more evident when looking at the integrated mass as a function of aperture radius. In order to better account for the asymmetric nature of the cluster, we set the centre of the aperture at the position of the two main galaxies (or BCGs). For each centre, we compute the projected mass within a given aperture as a function of the aperture radius. The resulting profiles are shown in Figure 4. All models agree well specially between $\approx$ 100–300 kpc, which is the range where lensing constraints are more abundant. At small radii ($r < 100$ kpc), the model in Cerny et al. (2018) predicts slightly more mass than our free-form models, specially in the SE clump. At radii larger than $\approx$ 400 kpc our free-form models falls below the prediction of the model of Cerny et al. (2018). This is an expected behaviour, since the free-form models usually assigns low masses to areas extending beyond the realm of the lensing constraints. This is simply a memory effect of the algorithm that does not constrain distant regions in the field of view, leaving their masses close to their initial value before the minimization (these masses are originally assigned small random values).

5. Discussion

The results from the previous section suggests that the mass in El Gordo is relatively well constrained in the inner 500 kpc region. Within this range, Cerny et al. (2018) finds that the masses within the 500 kpc radius for each clump have a mass ratio of 1.19 (for SE/NW). Compared with our results, we find that within the same radius, the SE/NW ratio is 0.98 for the driver model and 1.11 for the model with all systems. At 100 kpc, this ratio grows to 1.17 and 1.18 for the driver model and full model, respectively. This should be compared with the dynamical masses inferred in Menanteau et al. (2012), where for the SE/NW ratio (within the virial radius) they find a value of 0.6 ± 0.4, and hence consistent with a ratio of ~ 1 at 1σ with their measurement. The weak lensing analysis in Jee et al. (2014) finds a more discrepant ratio of the SE/NW groups (in the virial masses) of 0.56 ± 0.17 (statistical), in contrast with our results. This discrepancy may be due to systematic effects in either analysis, but it is also possible that the NW group becomes more massive than the SE group beyond the 500 kpc radius studied in the strong lensing analysis.

One of the more puzzling aspects of El Gordo cluster is the position of the X-ray emission in relation to the peak in the mass distribution. Botteon et al. (2016) study this cluster with X-rays and infers a very high velocity for the shock (with a Mach number of 3 or above), which is spatially coincident with one of the radio relics. Ng et al. (2015) combines different observations from El Gordo cluster to constrain the dynamical state of the cluster. Based on the separation of the two subgroups, the morphology of the radio relics and their polarization angle, they conclude that the cluster is most likely in a return phase. This naturally explains the relative position of the X-ray peak and the

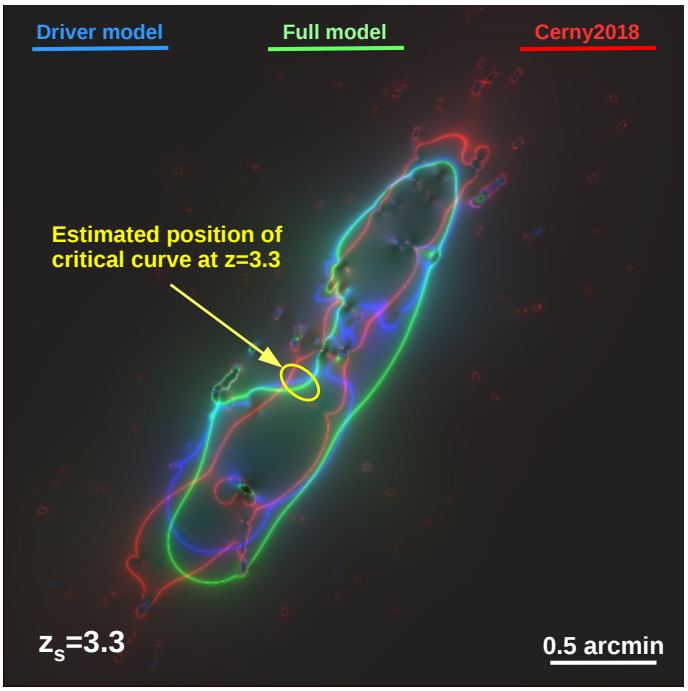

Fig. 6. Comparison of the critical curves between our models and the model in Cerny et al. (2018). The yellow ellipse marks the observed position of the critical curve from system 2 (at $z \approx 3.3$).

main BCG, which seems to be lagging behind the X-ray peak. Hallman & Markevitch (2004) studies the low-redshift cluster A168, which resembles El Gordo. Like in El Gordo, in A168 the peak of the X-ray emission seems to have moved ahead of the dominant galaxies in the cluster. They conclude that the "subcluster gas slingshots past the dark matter center, becomes unbound from the subcluster and expands adiabatically". This type of adiabatic expansion has been observed in N-body hydrodynamical simulations (Mathis et al. 2005), and it can result in a substantial cooling of the gas as it leaves the potential well. For a cluster in a return phase after a head-on collision, the gas leaves the potential well twice; a first time as it drags behind the peak of the mass distribution due to ram pressure, and a second time when the peak of the mass distribution falls back towards the centre of mass sprinting through the gas.

The results from our driver model seems to agree better with the Ng et al. (2015) interpretation (returning phase), since the X-ray peak is ahead of the mass peak. On the contrary, the full model seems to agree better with the interpretation of Molnar & Broadhurst (2015) and Zhang et al. (2015), since the mass peak coincides with the X-ray peak, and not with the BCG. This would suggest that the BCG was perturbed out from the potential well of the infalling cluster, which may be explained by the merging. Based on results from full N-body.hydro simulations (Molnar & Broadhurst 2015; Zhang et al. 2015), the infall velocity for El Gordo is not as large as for the Bullet cluster. If the velocity is not large enough, the ram pressure does not produce noticeable offsets between the mass and gas centers of the infalling cluster.

5.1. Total mass

We estimate the total mass within r_{200c} by fitting a projected NFW profile to the projected mass along the line of sight. We compute the integrated mass as a function of aperture radius taking as the centre of the cluster the actual centre of the FOV considered in this work, which is a position that falls right in between the two clumps. The integrated mass is shown in Figure 7 as a black solid line. Since the centre of the profile is taken in the middle point between the two subgroups, at small radii the integrated mass grows relatively slow with increasing radius. Only at radii larger than $\approx$ 400 kpc, the integrated mass shown in Figure 7 includes both clumps. At radii extending beyond the region where lensing constraints are available, our lensing code typically results in profiles which fall below an extrapolated NFW profile. This is a consequence of the lack of constrains in these regions, which translate in the final solution *remembering* the initial condition, typically values of the mass close to zero (see our earlier work for a detailed discussion of this memory effect Diego et al. 2005a, 2007). The memory effect can be appreciated in Figure 7 beyond radii$\approx$ 600 kpc. Given the asymmetry of the cluster and the extension of the lensing constraints, a fit to a symmetrical profile makes sense only in between these two radii (400–600 kpc). In Figure 7 we show three NFW profiles that are fit to the aperture mass profile in this range of radii. For each NFW model, we assume concentration value of $C = R_{\rm vir}/r_s = 6$ and vary only the scale radius. This value of the concentration is expected for clusters of masses similar to El Gordo. The dependency with the concentration is shown for the model with scale radius 250 kpc (dark blue dotted curves), where we vary the concentration between $C = 4.6$ and $C = 7.8$. The asymmetry of the cluster, together with the limited extension of the model in radius, does not allow us to get a good constraint on neither the concentration parameter nor the scale radius (with the consequent impact on the uncertainty due to the extrapolation), but the valid range of models predict a mass in the range $M_{200c} = (1.35\pm0.15)\times10^{15}M_\odot$ based on the extrapolation of suitable NFW profiles. This mass estimate is lower than previous estimates (by up to a factor $\approx$ 2.3 compared with the results in Jee et al. 2014), reducing the tension between the mass of this cluster and predictions from LCDM models. When compared with the simulated El Gordo cluster in Molnar & Broadhurst (2015) (black dashed line in Figure 7), the integrated mass profile shows a remarkably good agreement with the lens model (thick black line) below $\approx$ 500 kpc. Note that the simulated mass profile is not a fit to our reconstructed mass profile. Between $\approx$ 500 kpc and $\approx$ 700 kpc the simulated cluster increase the mass more rapidly than the lens model, suggesting that the scale radius in the simulated cluster is larger than 250 kpc. By fitting this regime in radius to an NFW profile, we infer a large core radius for the simulated cluster (light blue curve in Figure 7 with scale radius of 800 kpc and concentration parameter c=3). Extrapolation of the NFW profile, derived from fitting the simulated profile in the radii between $\approx$ 500 kpc and $\approx$ 700 kpc results in an overestimation of the M_{200c} mass by $\approx$ 60%, suggesting that our inferred M_{200c} mass for El Gordo cluster may be also overestimated, although the smaller scale radius of the NFW profiles used in this case should result in a smaller percentage of overestimation. The question of the total mass of El Gordo can not be settled until a proper joint analysis (combining strong lensing to break the mass-sheet degeneracy and weak lensing to cover the larger scales) is performed. As shown by the simulated cluster in Figure 7, extrapolations of a single analytical radial profile (where the analytical radial profile is constrained in range of radii) of a non-symmetric cluster can be unreliable.

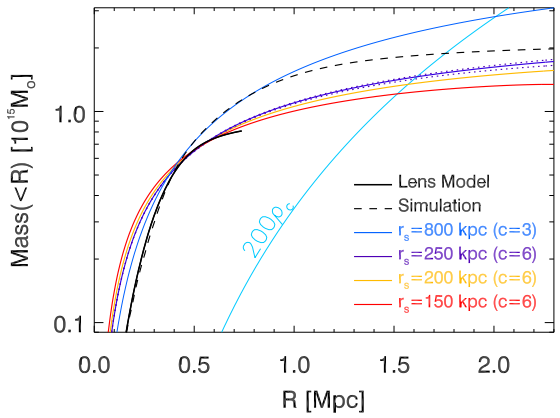

Fig. 7. The thick black solid line shows the integrated mass from the lens model as a function of aperture radius (i.e mas projected in a cylinder with radius R) when the centre is in the middle of the field of view (that is, in between the two clumps). The black-dashed line is the profile derived from the simulated "El Gordo" cluster in Molnar & Broadhurst (2015) when the center is chosen in the middle of the two subgroups (i.e like in the lens model profile). The three colored solid lines are the corresponding mass in the same aperture radius (i.e mass projected in a cylinder) for NFW profiles with concentration parameter $C = 6$ and scale radius between 150 kpc and 250 kpc. The two dotted blue lines are two alternative models with scale radius 250 kpc and concentration $C = 6 * 1.3$ and $C = 6/1.3$. The normalization is obtained after fitting the NFW profiles to the the black line in the range 400–600 kpc (see text for details). The light blue curve is the mass enclosed in a sphere with radius R and density 200 times the critical density (at the redshift of the cluster).

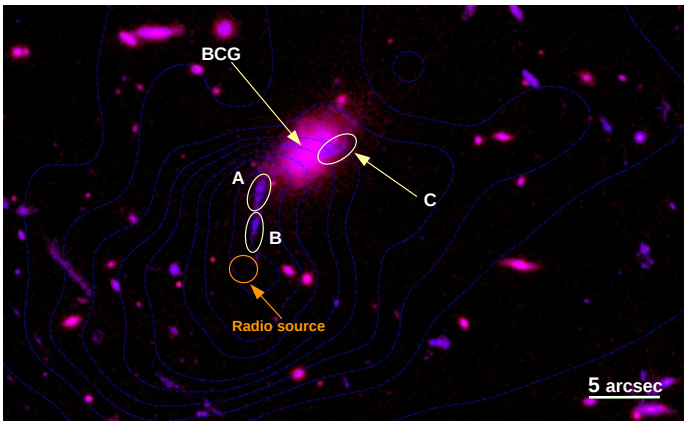

Fig. 8. UV feautures in EL Gordo. in The contours are the X-ray emission observed by Chandra. Feautres A,B and C are visible in the bluer HST bands and are marked with yellow ellipses. The orange circle marks the position of a compact radio source in Lindner et al. (2014).

5.2. The contribution from the gas and filamentary structure around the SE BCG

The position of the peak in the mass distribution of the full model is coincident with the peak in the X-ray emission. This coincidence raises the possibility that the X-ray emitting gas is contributing substantially to the projected mass in this region of the lens plane. Based on X-ray data, Menanteau et al. (2012) constraints the electron density to values between 0.023 cm^{-3} and 0.045 cm^{-3} within a region of diameter $\approx$ 170 kpc (or $\approx$ 22"). Based on this electron density, the gas surface mass density (projected on 170 kpc along the line of sight) is then $\Sigma_{gas} \approx 100 - 200 M_\odot$ pc^{-2}, which should be compared with the critical surface mass density of $\Sigma_{crit} = 2800 M_\odot$ pc^{-2} for a source at $z_s = 3$. The contribution from the gas to the convergence, κ (where κ is defined as the ratio between the surface mass density and the critical surface mass density at the given lens and source redshifts), projected along this relatively small interval of 170 kpc is 0.035-0.07. At the peak of the X-ray emission, and projecting over larger distances, the gas can easily contribute up to 0.1 to κ. This may be sufficient to explain the correlation between the total mass peak and the X-ray emission shown in Figure 3.

Interestingly, as discussed earlier, the peak of the X-ray emission coincides with blue features observed in the UV-optical bands (A and B in Figure 8). Based on the driver model, if these two features are multiply lensed objects they need to be at a redshift above $z = 1.8$. However, at this redshift, the predicted images would not form radially oriented arcs in our models, but rather tangential arcs. Radially oriented arcs at this position of the lens plane appear for redshifts $z > 2.5$, but the lens model can not reproduce arcs with a morphology similar to the observed ones. For redshifts between $z = 4.5$ and $z = 5.5$, counterimages for the arcs are expected at positions compatible with the three arclets of system 4. This correspondence explains the original classification of these features as part of system 4, but the morphology of the predicted images differ significantly from the observation, making this possibility unlikely. The two features are at distances of $\approx$ 35 and $\approx$ 50 kpc respectively from the centre of the BCG. The tight correlation shown in Figure 8 between these two features and the offset peak of the X-ray emission suggests that these two features may be the optical counterpart of a cooling flow (alternatively they could be associated with a jet emitting in UV-optical and X-rays). A well studied case that could serve as a similar example is the nearby cluster Abell 2597 (z=0.0821) where an arc-like feature correlates also very well with the peak in the X-ray emission. In Tremblay et al. (2012) they study this cluster combining data from X-ray, UV/optical, NIR and radio observations. They find evidence for a cooling flow in the X-ray band and filamentary features in the FUV and optical bands that resemble the blue features shown in Figure 8, which could be associated with precipitation of the gas (Voit et al. 2015).

Another remarkable example is Abell 1795, where the spatial correlation between the cooling flow and the FUV emission is even more clear. Bright structures visible in the UV/optical, but also in Ly-α (and Hα) emission, and around the BCGs are believed to contain active star forming regions with luminous and hot stars (Oonk et al. 2011). Oonk et al. (2011) suggest that contributions from stars are not sufficient to explain the FUV emission in Abell 2597, and that additional contributions from non-thermal processes should be considered. In Donahue et al. (2015), the authors study a larger sample of 25 BCGs in CLASH clusters spanning redshifts between $z = 0.206$ and $z = 0.890$. Similar filamentary features are found around several of the BCGs, some of them resembling the features seen around the BCG in El Gordo. Based on the similarity with the cold-gas structures produced in simulations of precipitation-driven active galactic nucleus feedback, in which jets uplift low-entropy gas to greater altitudes (Li & Bryan 2014; Li et al. 2015), they argue that AGN jets uplift the low-entropy gas, causing it to condense. In a similar study based on 10 cool-core BCGs, Mittal et al. (2015) argue that the cooling of the ICM contributes to the star formation in cool-core BCGs. Tremblay et al. (2015) study a sample of 16 cool-core BCGs at $z < 0.3$ (also exhibiting UV filamentary structure around the BCGs). They find that "nearly half

of the sample possesses kpc-scale filaments that, in projection, extend towards and around radio lobes and/or X-ray cavities", and conclude that the "filaments may have been uplifted by the propagating jet or buoyant X-ray bubble, or may have formed in situ by cloud collapse"

In this earlier work, the presence of an AGN is needed in order to power the uplifting mechanism. In the case of El Gordo, neither radio observations nor X-ray data support the hypothesis of an AGN at the centre of the BCG powering recent radio jets. Radio data reveal relics, but at a much larger distance from the BCG. Lindner et al. (2014) shows a compact radio source (named U7 in Figure 16 in their paper) at 75 kpc SE from the BCG, which is spatially coincident with the peak of the X-ray emission (see Figure 8). The peak of the emission in Chandra data is coincident with the position of the two blue features, and shows no evidence of point source emission at the centre of the BCG. One could argue that an AGN (i.e a SMBH) is ejected from the BCG, but this would imply an record breaking offset of $\approx$ 75 kpc, which is very difficult to explain with simulations, where typical offsets are in the range of $\approx$ 10 kpc at most. Instead, it may be more plausible that the UV/blue emission is a consequence of the cooling of the gas into large star forming regions, or that we are witnessing the tail of the X-ray radiation (bremstrahlung).

On the other hand, the other blue features observed around the BCG would agree also with the scenario discussed in earlier work (Donahue et al. 2015; Tremblay et al. 2015; Mittal et al. 2015), except for the fact that there is no sign of AGN at the centre of the galaxy (i.e., X-ray cavities around the BCG, or an X-ray point source at the centre of the BCG, or radio emission associated with the BCG).

6. Conclusions

We derive a new lens model for the El Gordo cluster using data from the RELICS program. We first derive a robust model (nicknamed the driver model) based on a reliable subsample of lensed galaxies. Using the driver model, we unveil new strongly lensed system candidates and infer their redshifts. With the full set of lens systems we derive an alternative model (or full model) for the mass distribution. Both models are similar to each other, but small differences can be identified, specially in the SE sector of the cluster. We explicitly compare our models with the one derived by Cerny et al. (2018) using the same RELICS data, but a different sample of lensed galaxies (although with substantial overlap between our sample and theirs). We find that our lens model predicts wider critical curves, but the integrated mass as a function of aperture is consistent with the model of Cerny et al. (2018). Our new model predicts also nearly twice the lensing efficiency above a given magnification factor (at large magnifications).

By fitting our full lens model to an NFW profile, and extrapolating up to R_{200c}, we find a mass $M_{200c} = (1.35\pm0.15)\times10^{15}\mathrm{M}_{\odot}$, where the uncertainty comes mostly from the poorly constrained scale radius (and to a lesser degree the concentration parameter). This mass estimate is smaller than previous estimates (by factors ranging from 1.3 to 2.3), relaxing the tension with standard LCDM models that predict that clusters with masses above $M_{200\rho} = 1.7\times10^{15}\mathrm{M}_{\odot}$ and at this redshift should be rare. We test the accuracy of the profile extrapolation using an N-body simulation that matches most of the observed features in El Gordo, and conclude that our mass estimate may still be overestimating the real mass due to an improper extrapolation of the profile. A combination of strong and weak lensing data should allow for a better constrain of the total mass of this cluster.

We find evidence for the lens model being sensitive to the gas mass. In particular, we find that the peak of the smooth component of the mass distribution in the full lens model agrees well with the peak of the X-ray emission (which is offset with respect to the nearby BCG). We discuss the possibility that two features at the location of these peaks, which are observed in the optical-UV bands, and interpreted in the past as background lensed galaxies, are instead the optical counterpart of a cooling flow, or a precipitation mechanism from the hot plasma.

The new lens model will be valuable when El Gordo is observed as part of of Cycle 1 of JWST. New arc systems, including several at high redshift are expected to be discovered with the new JWST data. Our reliable lens model will be used to identify new strongly lensed system candidates, as well as to estimate their redshifts.

Acknowledgements. J.M.D. acknowledges the support of projects AYA2015-64508-P (MINECO/FEDER, UE), funded by the Ministerio de Economia y Competitividad. This work was funded by NASA JWST Interdisciplinary Scientist grants NAG5-12460, NNX14AN10G, and 80NSSC18K0200 to RAW from GSFC. We would like to thank Harald Ebeling for making the code ASMOOTH (Ebeling et al. 2006) available. J.M.D. acknowledges the hospitality of the Physics Department at the University of Pennsylvania for hosting him during the preparation of this work. This work is based on observations made with the NASA/ESA *Hubble Space Telescope* and operated by the Association of Universities for Research in Astronomy, Inc. under NASA contract NAS 5-2655. Part of the data for this study is retrieved from the Mikulski Archive for Space Telescope (MAST). The authors would like to thank the RELICS team for making the reduced data set available to the community. The scientific results reported in this article are based in part on data obtained from the Chandra Data Archive [2][3][4].

References

Botteon, A., Gastaldello, F., Brunetti, G., & Kale, R. 2016, MNRAS, 463, 1534
Cerny, C., Sharon, K., Andrade-Santos, F., et al. 2018, ApJ, 859, 159
Coe, D., Salmon, B., Bradac, M., et al. 2019, arXiv e-prints [arXiv:1903.02002]
Diego, J. M. 2018, arXiv e-prints [arXiv:1806.04668]
Diego, J. M., Broadhurst, T., Chen, C., et al. 2016, MNRAS, 456, 356
Diego, J. M., Kaiser, N., Broadhurst, T., et al. 2018, ApJ, 857, 25
Diego, J. M., Protopapas, P., Sandvik, H. B., & Tegmark, M. 2005a, MNRAS, 360, 477
Diego, J. M., Tegmark, M., Protopapas, P., & Sandvik, H. B. 2007, MNRAS, 375, 958
Donahue, M., Connor, T., Fogarty, K., et al. 2015, ApJ, 805, 177
Donnert, J. M. F. 2014, MNRAS, 438, 1971
Ebeling, H., White, D. A., & Rangarajan, F. V. N. 2006, MNRAS, 368, 65
Hallman, E. J. & Markevitch, M. 2004, ApJ, 610, L81
Harrison, I. & Coles, P. 2012, MNRAS, 421, L19
Jee, M. J., Hughes, J. P., Menanteau, F., et al. 2014, ApJ, 785, 20
Kelly, P. L., Diego, J. M., Rodney, S., et al. 2018, Nature Astronomy, 2, 334
Li, Y. & Bryan, G. L. 2014, ApJ, 789, 54
Li, Y., Bryan, G. L., Ruszkowski, M., et al. 2015, ApJ, 811, 73
Lindner, R. R., Baker, A. J., Hughes, J. P., et al. 2014, ApJ, 786, 49
Mathis, H., Lavaux, G., Diego, J. M., & Silk, J. 2005, MNRAS, 357, 801
Menanteau, F., Hughes, J. P., Sifón, C., et al. 2012, ApJ, 748, 7
Mittal, R., Whelan, J. T., & Combes, F. 2015, MNRAS, 450, 2564
Molnar, S. M. & Broadhurst, T. 2015, ApJ, 800, 37
Molnar, S. M. & Broadhurst, T. 2018, ApJ, 862, 112
Ng, K. Y., Dawson, W. A., Wittman, D., et al. 2015, MNRAS, 453, 1531
Oonk, J. B. R., Hatch, N. A., Jaffe, W., Bremer, M. N., & van Weeren, R. J. 2011, MNRAS, 414, 2309
Sendra, I., Diego, J. M., Broadhurst, T., & Lazkoz, R. 2014, MNRAS, 437, 2642
Tremblay, G. R., O'Dea, C. P., Baum, S. A., et al. 2012, MNRAS, 424, 1042
Tremblay, G. R., O'Dea, C. P., Baum, S. A., et al. 2015, MNRAS, 451, 3768

[2] ivo://ADS/Sa.CXO#obs/12258
[3] ivo://ADS/Sa.CXO#obs/14022
[4] ivo://ADS/Sa.CXO#obs/14023

Voit, G. M., Donahue, M., Bryan, G. L., & McDonald, M. 2015, Nature, 519, 203
Waizmann, J.-C., Ettori, S., & Moscardini, L. 2012, MNRAS, 420, 1754
Watson, W. A., Iliev, I. T., Diego, J. M., et al. 2014, MNRAS, 437, 3776
Williamson, R., Benson, B. A., High, F. W., et al. 2011, ApJ, 738, 139
Windhorst, R. A., Timmes, F. X., Wyithe, J. S. B., et al. 2018, ApJS, 234, 41
Zhang, C., Yu, Q., & Lu, Y. 2015, ApJ, 813, 129
Zhang, C., Yu, Q., & Lu, Y. 2018, ApJ, 855, 36
Zitrin, A., Menanteau, F., Hughes, J. P., et al. 2013, ApJ, 770, L15

Appendix A: Compilation of arc positions

This appendix presents the sample of secure and likely lensed multiple images detected behind El Gordo using the updated imaging from the RELICS program. Table A.1 lists the complete sample of images and their redshifts assigning IDs to each of them.

The first column shows system ID following the original notation of Zitrin et al. (2013) (ID1.ID2.ID3 = System.Image.Knot) and ranks (A, B and C) . Systems 1-4 were initially presented by Zitrin et al. (2013). IDs marked with bold face are new systems presented in this work. Photometric redshifts are given in column $z_{\rm phot}$. The systems having spectroscopic redshift are marked with bold face. Redshifts predicted by the lens model are given in column $z_{\rm model}$. The redshift used to reconstruct the lens are given in column $z_{\rm used}$.

The column labeled Rank shows the quality of the system. Systems marked with rank A are very reliable and are used to derive the *driver* model. Systems marked with B are used to derive (together with systems having rank A) the *full* model. Systems marked with C are less reliable, but still highly consistent with the driver lens model. In the last column 1, 2 and 3 refer to previous work, where these systems are defined. Z13 stands for Zitrin et al. (2013) while C18 for Cerny et al. (2018). The number in parenthesis next to the reference indicates the system ID in the corresponding publication.

Table A.1. Full strong lensing data set. See text for description of the columns. For the photometric redshifts we indicate the range of redshifts (from multiple images) after excluding extreme values. Systems marked in bold face are newly identified systems.

KnotID	RA	DEC	$z_{\rm phot}$	$z_{\rm model}$	$z_{\rm used}$	Rank	Comments
1.1.1	1 02 53.275	-49 15 16.49		3.0	3.0	A	Z13(1)
1.2.1	1 02 52.819	-49 15 18.29	2.93			A	
1.3.1	1 02 55.411	-49 14 59.90				A	
1.1.2	1 02 53.340	-49 15 16.36				A	
1.2.2	1 02 52.763	-49 15 18.70	2.8			A	
1.3.2	1 02 55.391	-49 15 00.33	2.91			A	
1.1.3	1 02 53.480	-49 15 16.01				A	
1.2.3	1 02 52.600	-49 15 19.68				A	
1.3.3	1 02 55.320	-49 15 01.18	3.26			A	
2.1.1	1 02 55.828	-49 15 52.37	3.21	3.3	3.3	A	Z13(2)
2.2.1	1 02 56.749	-49 15 46.01	3.39			A	
2.3.1	1 02 54.429	-49 16 04.63	3.3			A	
2.1.2	1 02 55.671	-49 15 53.54				A	
2.2.2	1 02 56.885	-49 15 45.17	3.27			A	
2.3.2	1 02 54.456	-49 16 04.00	2.9			A	
2.1.3	1 02 55.983	-49 15 51.24				A	
2.2.3	1 02 56.573	-49 15 47.06				A	
2.3.3	1 02 54.383	-49 16 04.61				A	
3.1.1	1 02 56.257	-49 15 07.03		4.4	4.4	A	Z13(3)
3.2.1	1 02 54.751	-49 15 19.54				A	
3.3.1	1 02 51.536	-49 15 38.47	4.54			A	
4.1.1	1 02 59.986	-49 15 49.54	3.98	3.2	4.0	A	Z13(4)
4.2.1	1 02 55.362	-49 16 26.09	4.0			A	
4.3.1	1 02 56.599	-49 16 08.45				A	
5.1.1	1 02 54.539	-49 14 58.60	2.4	2.8	2.8	A	C18(13)
5.2.1	1 02 53.230	-49 15 07.11				A	
5.3.1	1 02 51.803	-49 15 17.05	2.2,2.5			A	
6.1.1	1 02 55.484	-49 15 05.04		4.3	4.3	B	
6.2.1	1 02 55.067	-49 15 09.84		4.3		B	
6.3.1	1 02 51.242	-49 15 37.08	4.3,4.5	4.3		C	
6.1.2	1 02 55.330	-49 15 05.70				B	
6.2.2	1 02 55.134	-49 15 07.80				B	
6.3.2	1 02 51.193	-49 15 37.08				C	
7.1.1	1 02 55.477	-49 16 07.32	4.53	4.5		B	Z13
7.2.1	1 02 54.927	-49 16 14.85				B	
7.3.1	1 02 59.321	-49 15 44.52	4.8			C	
8.1.1	1 02 55.836	-49 16 07.56	3.55	4.0	3.5	D	Z13
8.2.1	1 02 55.211	-49 16 16.10				D	
9.1.1	1 02 56.288	-49 16 07.90	2.72	3.0	2.9	B	Z13
9.2.1	1 02 55.641	-49 16 17.54	2.26			B	
9.3.1	1 02 59.043	-49 15 53.35	2.32			C	
10.1.1	1 02 55.784	-49 15 13.91	5.1	5.15	5.1	B	
10.2.1	1 02 55.558	-49 15 15.99				B	
10.3.1	1 02 51.772	-49 15 44.75				C	
11.1.1	1 02 59.612	-49 16 26.61	2.19	3.1	2.2	B	Z13(5)
11.2.1	1 02 59.467	-49 16 27.99				B	
11.3.1	1 02 57.774	-49 16 39.10				B	
12.1.1	1 02 54.571	-49 14 54.16	3.36	3	3.0	B	C18(14)
12.2.1	1 02 53.021	-49 15 04.94				B	
12.3.1	1 02 51.782	-49 15 14.38	2.8			B	
13.1.1	1 02 59.884	-49 16 30.53		2.4	3.0	B	
13.2.1	1 02 59.719	-49 16 32.59				B	
14.1.1	1 03 00.135	-49 15 46.29	2.74	4	4.0	B	
14.2.1	1 02 55.161	-49 16 23.07		4		B	
14.3.1	1 02 56.331	-49 16 08.55				B	

Table A.2. cont.

KnotID	RA	DEC	z_{phot}	$z_{\rm model}$	$z_{\rm used}$	Rank	Comments
15.1.1	1 02 58.512	-49 16 37.00	2.7	2.65	2.7	B	C18(5)
15.2.1	1 02 58.736	-49 16 35.71	2.8			B	
15.3.1	1 03 00.100	-49 16 21.12				C	
16.1.1	1 02 58.017	-49 15 33.48		4.3	4.1	B	
16.2.1	1 02 55.237	-49 15 53.35				B	
16.3.1	1 02 53.719	-49 16 01.99	4.13			B	
17.1.1	1 02 55.546	-49 14 58.28		4.6	4.6	C	
17.2.1	1 02 54.693	-49 15 04.33				C	
17.3.1	1 02 50.950	-49 15 33.57	4.4			C	
18.1.1	1 02 57.018	-49 15 47.45		3.4	3.3	C	
18.2.1	1 02 55.784	-49 15 56.22	3.27			C	
18.3.1	1 02 54.575	-49 16 06.89				C	
19.1.1	1 02 52.709	-49 15 51.82		4.5	5.0	C	
19.2.1	1 02 55.275	-49 15 33.43				C	
19.3.1	1 02 56.886	-49 15 21.16				C	